A near-infrared AIE fluorescent probe for myelin imaging: From sciatic nerve to the optically cleared brain tissue in 3D

Ming-Yu Wu[a,b,1], Alex Y. H. Wong[a,1] , Jong-Kai Leung[a], Chuen Kam[a], Kenneth Lap-Kei Wu[c] , Ying-Shing Chan[c], Kai Liu[d,e], Nancy Y. Ip[d,e] , and Sijie Chen[a,2]

[a]Ming Wai Lau Centre for Reparative Medicine, Karolinska Institutet, Hong Kong, China; [b]School of Life Science and Engineering, Southwest Jiaotong University, Chengdu 610031, China; [c]School of Biomedical Sciences, Li Ka Shing Faculty of Medicine, and State Key Laboratory of Brain and Cognitive Sciences, The University of Hong Kong, Hong Kong, China; [d]Division of Life Science, State Key Laboratory of Molecular Neuroscience, The Hong Kong University of Science and Technology, Hong Kong, China; and [e]Hong Kong Center for Neurodegenerative Diseases, Hong Kong, China

Myelin, the structure that surrounds and insulates neuronal axons, is an important component of the central nervous system. The visualization of the myelinated fibers in brain tissues can largely facilitate the diagnosis of myelin-related diseases and understand how the brain functions. However, the most widely used fluorescent probes for myelin visualization, such as Vybrant DiD and FluoroMyelin, have strong background staining, low-staining contrast, and low brightness. These drawbacks may originate from their self-quenching properties and greatly limit their applications in three-dimensional (3D) imaging and myelin tracing. Chemical probes for the fluorescence imaging of myelin in 3D, especially in optically cleared tissue, are highly desirable but rarely reported. We herein developed a near-infrared aggregation-induced emission (AIE)-active probe, PM-ML, for high-performance myelin imaging. PM-ML is plasma membrane targeting with good photostability. It could specifically label myelinated fibers in teased sciatic nerves and mouse brain tissues with a high–signal-to-background ratio. PM-ML could be used for 3D visualization of myelin sheaths, myelinated fibers, and fascicles with high-penetration depth. The staining is compatible with different brain tissue–clearing methods, such as Clear[T] and Clear[T2]. The utility of PM-ML staining in demyelinating disease studies was demonstrated using the mouse model of multiple sclerosis. Together, this work provides an important tool for high-quality myelin visualization across scales, which may greatly contribute to the study of myelin-related diseases.

myelin imaging | aggregation-induced emission | plasma membrane | near infrared | brain tissue imaging

Myelination, which involves the ensheathment of axons by oligodendrocytes in the central nervous system (CNS) or Schwann cells in the peripheral nervous system (PNS), is an evolutionary advantage to the complex nervous system of vertebrates (1, 2). By wrapping glial membranes around axons, axonal insulation facilitates saltatory conduction up to 100-fold compared to unmyelinated axons (3, 4). Additionally, the architecture of axo-glial junctions creates polarized domains for protein segmentation, thus allowing the local clustering of ion channels and the corresponding downstream signaling, as well as the accumulation of scaffolding and cytoskeletal proteins for axonal transport (5, 6). Given the unique axo-glial organization and its functions, the demyelination in neurological disorders, such as multiple sclerosis and leukodystrophies, is associated with progressive axonal loss, cognitive impairment, and motor symptoms (7–11). Myelin imaging is therefore considered as not only an approach for diagnosing neuropathies but also a research tool to understand the mechanism underlying demyelinating diseases (12, 13).

Provided that billions of neurons are densely populated in the brain with myelinated nerve fibers projected to the inner part of the brain, labeling tools enabling deep-tissue imaging with high spatial resolution will greatly facilitate the reconstruction of neural networks in three-dimension (3D) (14, 15). Some label-free imaging techniques, such as spectral confocal reflectance microscopy (14), coherent anti-Stokes Raman scattering (16), third-harmonic generation (17), and optical coherence tomography (OCT) (18), are developed to offer powerful methodological toolboxes for uncovering mechanisms of myelin generation and neuroplasticity in the live brain. On the other hand, fluorescence imaging is an indispensable technique for visualizing biological molecules and structures, as well as tracking changes in distribution, morphology, and the intensity of the target of interest with a higher spatial resolution. It is also widely used for myelin imaging (19). Immunofluorescence staining, fluorescent protein labeling, and small-molecule fluorescent probe staining are three commonly used methods for fluorescence biostaining and imaging. Compared with the immunostaining and genetically encoded fluorescent protein

> **Significance**
>
> The high spatial resolution of three-dimensional (3D) fluorescence imaging of myelinated fibers will greatly facilitate the understanding of 3D neural networks and the pathophysiology of demyelinating diseases. However, existing myelin probes are far from satisfactory because of their low–signal-to-background ratio and poor tissue permeability. We herein developed a near-infrared aggregation-induced emission-active probe, PM-ML, for high-performance myelin imaging. PM-ML could specifically image myelinated fibers in teased sciatic nerves and mouse brain tissues with high contrast, good photostability, and deep penetration depth. PM-ML staining is compatible with several tissue-clearing methods. Its application in assessing myelination for neuropathological studies was also demonstrated using a multiple sclerosis mouse model.

CHEMISTRY

NEUROSCIENCE

labeling, which involves tedious and time-consuming sample preparation procedures, small-molecule fluorescent probe staining offers a uniquely reliable and feasible method for brain tissue staining and imaging (20). The relatively small size, low costs, ease of use, and reliability of small-molecule fluorescent probes are advantageous to visualize morphological details in tissues, especially for 3D tissues (21). Generally, an ideal probe for deep-tissue imaging should have the following characteristics: 1) near-infrared (NIR) emission with a high-penetration depth and low interference from biological auto-fluorescence; 2) targetability to a desired structure or molecule; 3) bright and photostable; 4) adaptable to multiplexed tissue interrogation; and 5) easy to synthesis and use (20). Despite that currently available commercial myelin-specific fluorescent probes, such as sulforhodamine 101, Vybrant DiD (DiD), and FluoroMyelin Green/Red, are widely used, they have shortcomings in different degrees of background staining, low-staining contrast, low brightness, and poor tissue permeability (22–27). Actually, sulforhodamine 101 is more commonly used in labeling astrocytes (28). While lipophilic probes, such as DiD and FluoroMyelin Green/Red, stain the membranes of the cells and thus have a high concentration of dye accumulated in the myelin structures, which are formed by multilamellar membrane wrapping (29). This contributes to the myelin selectivity of these probes, but the high concentration of these probes in myelin at the same time may lead to fluorescence self-quenching, resulting in a low–signal-to-background ratio (30). Though advanced microscopy and tissue-clearing methods are developed in achieving better imaging quality, unoptimized probes hinder high-quality imaging and the tracking of myelinated axons in deep brain. Currently, there is only one reported case of deep-tissue myelin imaging using the chemical probe (23). This method uses the commercial probe, DiD, which has a poor tissue permeability so that the pretreatment of the tissues with Triton X-100 is required to facilitate dye penetration. The pretreatment step, however, also washes away the lipids and destroys some fine structures of myelin, thus greatly reducing the myelin selectivity of the staining (20). Therefore, fluorescent probes for 3D myelin imaging with good selectivity, high–signal-to-background ratio, good tissue permeability, and tissue-clearing compatibility are highly desirable.

In recent years, fluorescent probes with aggregation-induced emission (AIE) properties have emerged as a group of excellent candidates for bioimaging (31–34). AIE luminogens (AIE-gens) show weak emission in dilute solution but emit strongly in the aggregated state, which offers low background fluorescence, strong signal-to-background ratio, and good photostability in practical bioimaging (35–38). With the rational molecular designs, AIE-based NIR materials offer superior performance in biomolecular imaging and tracing (39–41). However, tissue bioimaging using AIE materials currently are mostly focused on tumor imaging, vascular imaging, and lymphatic imaging. The application of AIE materials in neuroimaging remains to be explored. This prompts us to develop a type of NIR AIE probes for 3D myelin imaging in brain tissues.

Different from the plasma membrane of eukaryotic cells, which contains about 40% of lipids, the myelin membrane contains as many as 70% of lipids (42, 43). Therefore, targeting the plasma membrane lipids is a feasible approach for the designing of the myelin-specific probe (23). Based on this postulation, we developed a fluorescent probe, named PM-ML, for myelin imaging. PM-ML showed AIE properties with NIR emission. It specifically labeled the plasma membrane in live and fixed cells with excellent photostability. Compared with the commercial myelin probes FluoroMyelin Red and DiD, PM-ML selectively stained myelinated regions in the brain of wild-type (WT) mice with a high–signal-to-background ratio. Furthermore, it could be used for 3D myelin imaging in mouse brain tissues with

good tissue penetration and high specificity. We also demonstrated a lack of myelination in hypomyelinated *shiverer* mutant mice by using PM-ML.

Results and Discussion

Design and Synthesis of PM-ML. Our molecular design of the probe was mainly based on three considerations: NIR emission, plasma membrane targeting, and the nonplanar conformation for the AIE attribute. It is known that intramolecular charge transfer with D–π–A structures, which results in lower electronic band gaps, is generally an efficient and widely used strategy to design NIR probes (44). To target the plasma membrane, an amphiphilic structure mimicking the structure of phospholipids in the membrane is preferred (36). Based on these considerations, the molecular structure that PM-ML adopted was featured with a triphenylamine (TPA) segment and bithiophene serving as the electron donor, the bithiophene and carbon–carbon double bond functioning as the π-bridge, and the pyridinium acting as an electron acceptor (Fig. 1*A*). This molecular design constructed a D–π–A structure. Besides, the nonplanar TPA units and the overall bended conformation of PM-ML formed the structural foundation for its AIE attributes. Furthermore, the donor and the π-bridge of PM-ML are hydrophobic in nature, which can be embedded into the nonpolar hydrocarbon tails of phospholipids through hydrophobic interactions, while the acceptor pyridinium salt is hydrophilic and positively charged, which retains its molecular orientation facing outwards to the lipid bilayers and binds to the negatively charged phosphate group of phospholipids through strong electrostatic interactions. These together contribute to the plasma membranes targetability of PM-ML (Fig. 1*A*) (45). Accordingly, PM-ML was synthesized through a simple condensation reaction of an aldehyde with pyridinium and anion-exchanging reaction (*SI Appendix*) with 86% yield, which was characterized by ^{1}H NMR, ^{13}C NMR, and high-resolution mass spectrometry (*SI Appendix*, Figs. S1–S3).

Photophysical Properties of PM-ML. The optical properties of PM-ML were investigated by photoluminescence spectrometry. It showed the maximum absorption peak at 495 nm in dimethyl sulfoxide (DMSO) and emission at 708 nm in solid state with a 213-nm Stokes shift (Fig. 1*B*). We then used a mixed solvent consisting of DMSO and different fractions of toluene (DMSO/PhMe) as the solvent system to evaluate its AIE properties. As shown in Fig. 1 *C* and *D*, PM-ML showed almost no emission in pure DMSO solution with a quantum yield (QY) of 0.05% and very weak NIR emission when the PhMe fraction (f_T) was below 80%. Further increasing f_T beyond 80% led to an aggregate formation with a quick enhancement of the emission and a blue-shifted maximum emission from 705 to 670 nm. The fluorescence intensity of PM-ML in 99.9% PhMe solution was 214-fold higher than that in pure DMSO, and the QY increased to 8.5% (Fig. 1*D*). The aggregate formation was confirmed by dynamic light scattering with an average size of 277.5 nm (Fig. 1*E*). As a result, these data affirmatively indicated the typical AIE properties of PM-ML.

The binding capacity of PM-ML with phospholipids was investigated with photoluminescence spectrometry. 1,2-dioleoyl-sn-glycero-3-phosphocholine (DOPC) and 2-oleoyl-1-palmitoyl-sn-glycero-3-phosphocholine (POPC) are the two commonly used model phospholipids for cell membrane lipids. Upon binding to phospholipid structures, the emitting moieties of PM-ML are embedded into the phospholipids, which restricts the intramolecular motion of PM-ML. As shown in Fig. 1*F*, this gave rise to its strong NIR emission with a hypsochromic shift from 700 to 640 nm, accompanied with a 94.1- and 196.8-fold increase in emission intensity in the presence of DOPC and POPC, respectively.
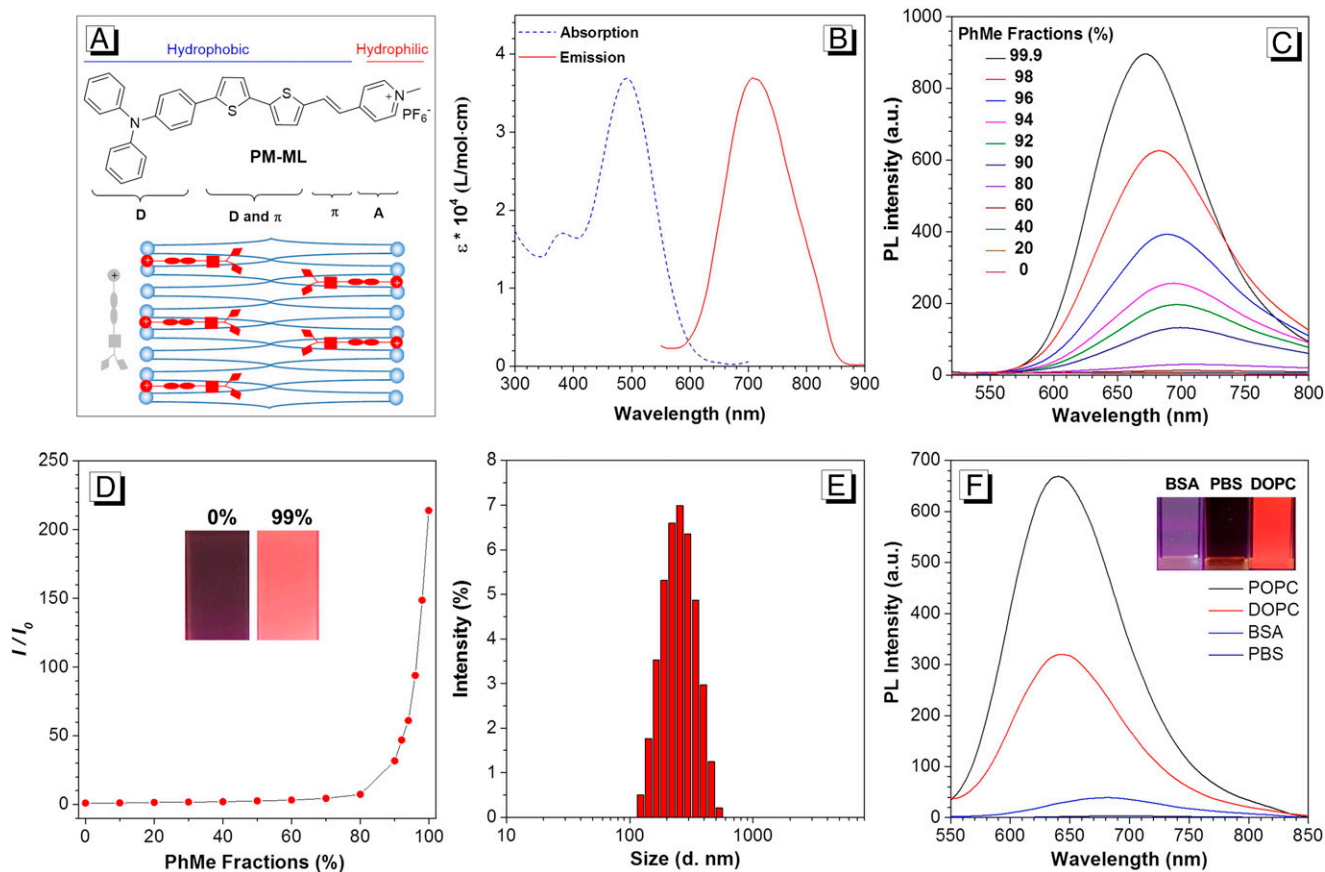
Fig. 1. Structure and photophysical properties of PM-ML. (*A*) The chemical structure, schematic illustration of PM-ML structural characteristics, and its interaction with membrane structure. (*B*) The molar absorption coefficient of PM-ML in DMSO and its emission spectrum in the solid state. (*C*) Photoluminescence (PL) spectra of PM-ML (10 μM) in the mixtures of DMSO and toluene (PhMe) with different PhMe fractions. (*D*) The plot of the relative emission intensity of PM-ML versus PhMe fractions. I_0 and I are the peak values of PL intensities of PM-ML in DMSO and DMSO/PhMe mixtures, respectively. (*Inset*) Fluorescence images of PM-ML in DMSO solution (0% PhMe) and aggregated state (99% PhMe) with 365-nm excitation. (*E*) Size distribution of PM-ML in the mixture of DMSO/PhMe with 99% PhMe content measured by dynamic light scattering. (*F*) PL spectra of PM-ML (10 μM) in phosphate-buffered saline (PBS) solution with 3 mg · mL^{-1} phospholipids (POPC or DOPC) or proteins (BSA). (*Inset*) Corresponding fluorescence images of PM-ML in PBS solution, DOPC, or BSA under a hand-held ultraviolet lamp at 365 nm.

Bovine serum albumin (BSA), which contains hydrophobic binding sites in its native folding structure, can activate the fluorescence of many water soluble/amphiphilic AIEgens (46, 47). Our experiment shows that BSA could only marginally turn on the fluorescence of PM-ML (Fig. 1*F*).

Plasma Membrane Targetability of PM-ML. Ascribing to the AIE properties, amphiphilicity (log P: 4.384), and the strong phospholipid binding of PM-ML, we then examined its subcellular localization in live and fixed mammalian cell lines. In HeLa (*SI Appendix*, Fig. S4 and Fig. 2), RAW264.7, and NIH 3T3 cells (*SI Appendix*, Fig. S5), PM-ML labeled cell surface regions, which colocalized well with the commercial plasma membrane probe CellMask Green. The high Pearson's correlation coefficient of 0.93 suggests its labeling specificity to the plasma membrane. Meanwhile, PM-ML was biocompatible to HeLa cells, which showed low cytotoxicity in the standard MTT assays (*SI Appendix*, Fig. S6). PM-ML also had high photostability under consecutive confocal imaging. Compared to CellMask Green, which lost ∼40% of fluorescence intensity after 100 scans, PM-ML retained ∼90% of fluorescence intensity at the end of the scanning (*SI Appendix*, Fig. S7). Together, PM-ML is a plasma membrane–specific probe with superior biocompatibility and photostability.

PM-ML Labels Myelin Sheath in Teased Sciatic Nerve Fibers from the PNS. Sciatic nerve fibers in the PNS are wrapped around by Schwann cells (Fig. 3*A*) (48). This multilayered, membrane-rich myelin sheath is therefore a plausible target of PM-ML. To test this possibility, mouse-teased sciatic nerve fibers were stained with PM-ML. Under the confocal microscope, we clearly observed that PM-ML labeled the edge of teased sciatic nerve fibers (Fig. 3*B*). Schmidt–Lanterman incisures and the node of Ranvier are the structures of Schwann cells in which the plasma membrane is not tightly wrapped and absent, respectively (49). By highlighting the edge of teased sciatic nerve fibers with PM-ML, histological structures of Schmidt–Lanterman incisures and the node of Ranvier could be identified along the nerve fibers at high magnification (Fig. 3*C*). This is consistent with our hypothesis that PM-ML labeled myelin sheath via the tightly wrapped plasma membrane of Schwann cells.

Myelin Labeling of Brain Tissues by PM-ML. In the brain, the cerebral cortex is organized into the outermost molecular layer, consisting of parallel fibers, inhibitory interneurons and unmyelinated dendrite of the Purkinje cells, the middle Purkinje layer containing cell bodies of Purkinje cells, and the innermost granular layer (GL) where Golgi cells and granule cells reside (50). In the deeper area of cerebrum and cerebellum (CB), it consists largely of myelinated axons and oligodendrocytes, which are known as white matter (wm) (51). To further validate the ability of myelin labeling in the CNS by PM-ML, the cryosection of corpus callosum (CC), which are rich in myelinated nerve fibers, or CB were costained with PM-ML and the commercial myelin probe FluoroMyelin Green (*SI Appendix*,
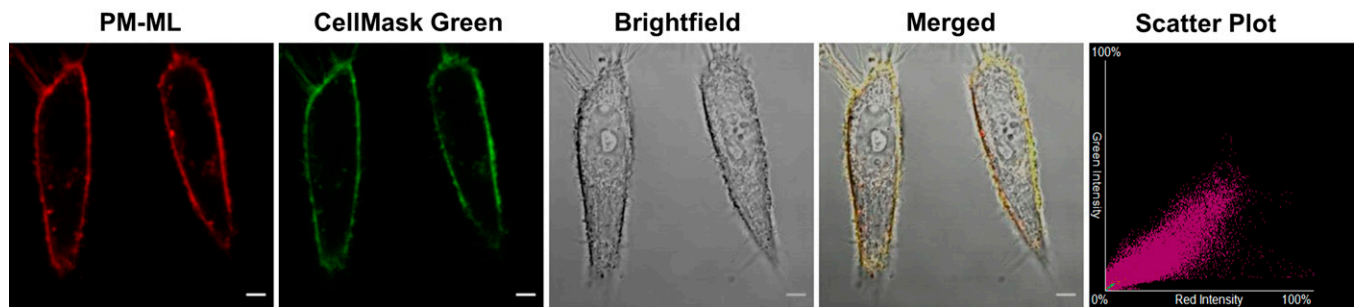
Wu et al.
A near-infrared AIE fluorescent probe for myelin imaging: From sciatic nerve to the optically cleared brain tissue in 3D

PNAS | 3 of 9
https://doi.org/10.1073/pnas.2106143118

CHEMISTRY

NEUROSCIENCE

Fig. 2. PM-ML labeled the plasma membrane of HeLa cells. HeLa cells labeled with PM-ML (red) and CellMask Green (green) were imaged under bright-field and confocal imaging. The fluorescence signal from both channels overlaid with each other (yellow) with a high Pearson's correlation coefficient of 0.93, as shown in the scatter plot. (Scale bars, 5 μm.)

Fig. S8 and Fig. 4*A*). Confocal imaging showed that the fluorescence signal from both probes overlaid with each other with high Pearson's correlation coefficient.

To further evaluate the suitability of PM-ML for the high-quality 3D fluorescence imaging of myelinated fibers, we compared the staining performance of PM-ML with that of the reported myelin probes. Till now, the only reported probe for the 3D imaging of myelin was DiD. However, DiD itself has poor tissue permeability and needs Triton X-100 (0.1%) for permeabilization, which potentially extracts lipids and destroys the fine structures of myelin (20). As shown in *SI Appendix*, Fig. S9 and Movie S1, DiD had very low-myelin selectivity and tissue permeability in untreated brain tissues. Compared with FluoroMyelin Red and DiD, PM-ML was much brighter under the same laser power (*SI Appendix*, Fig. S10). Importantly, PM-ML showed less fluorescence background than FluoroMyelin Red and DiD (Fig. 4*B* and *SI Appendix*, Figs. S11–S13). The

single labeling of mouse cleared tissues with PM-ML showed intense fluorescence signal in the CB, striatum (STR), and CC regions, which had a higher–signal-to-background ratio than the single labeling with FluoroMyelin Red and DiD. We postulate that one of the reasons for the good contrast of PM-ML staining in myelin in fixed tissue samples may arise from its good plasma membrane selectivity in fixed cells. As shown in *SI Appendix*, Figs. S14 and S15, cell membrane probes, such as Pent-TMP (36), CellMask Green, and FluoroMyelin Green/Red, almost had no selectivity to the plasma membrane in fixed cells. Compared with DiD, PM-ML also demonstrated better plasma membrane–staining performance and had a higher–signal-to-background ratio.

To demonstrate the superiority of PM-ML in imaging myelin sheaths, the 3D fluorescence imaging of myelin in brain tissues from young mice (P18) was carried out with PM-ML or Fluoro-Myelin Red/Green. As shown in Fig. 4*C*, fibers in caudate putamen (CPu) labeled by PM-ML clearly showed myelination in parallel along individual nerve fibers. In a 3D reconstructed image with an imaging depth of 60 μm, axonal fibers grouped together in discrete fascicles could be identified with high–signal-to-background ratio. In comparison, the myelin structures labeled by FluoroMyelin Red/Green were with a low contrast. The high–background fluorescence signal of Fluoro-Myelin probes made it difficult to identify individual nerve fascicles and trace axonal bundles at a high density (Fig. 4*C* and Movies S2–S6).

Visualizing the Entire Myelinated Fiber Tracts in Brain Tissues. Visualizing myelinated fibers in 3D space with a high-resolution fluorescence microscope can provide valuable insights into the topological organization of brain connectivity which are highly beneficial to neurological studies (14). Moreover, tracking the fiber distribution in animal models can aid in the development of treatments for demyelinating diseases and the assessment of their therapeutic effectiveness (15). Taking advantage of high-labeling specificity and the high–signal-to-background ratio of PM-ML in myelin labeling, we sought to apply PM-ML for the 3D visualization of myelinated fiber tracts in thick brain sections. First, we applied PM-ML for myelin labeling in an intact 1-mm thick mouse sagittal brain section cleared with the *Clear*[T] (Fig. 5*A* and Movie S7) or *Clear*[T2] (*SI Appendix*, Fig. S16*A*) method. The stitched image from 3D reconstruction showed the labeling of myelinated fiber tracts and fascicles in different brain regions (Fig. 5 *B–E* and *SI Appendix*, Fig. S16*B*). We could identify wm tracts, such as the cingulum bundle along the CC, the splenium of the CC, dorsal/ventral hippocampal commissure and fornix connecting to hippocampus, mammillothalamic tract and stria medullaris thalami in close proximity to thalamus, and the anterior commissure (aco). Several brain regions showing myelinated nerve fibers could also be
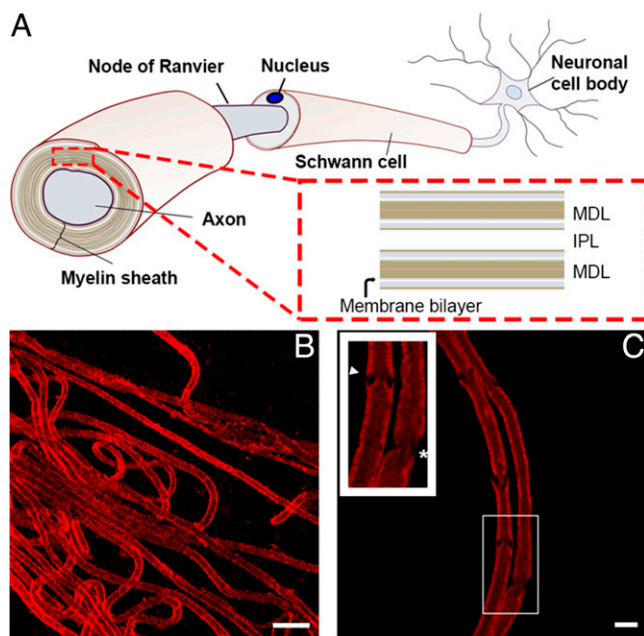

Fig. 3. Labeling of myelin sheath in teased sciatic nerve fibers from the PNS by PM-ML. (*A*) Schematic diagram of an axon in the sciatic nerve myelinated by Schwann cells. MDL, major dense line and IPL, intraperiod line. (*B*) Confocal image of fixed teased sciatic nerve fibers from C57BL/6J mice stained with PM-ML at 20× magnification. (Scale bar, 20 μm.) (*C*) A segment of teased sciatic nerve fibers. The inset is enlarged from the region of interest (white rectangle). It shows Schmidt–Lanterman incisures (arrowhead) and node of Ranvier (asterisk). (Scale bar, 5 μm.)
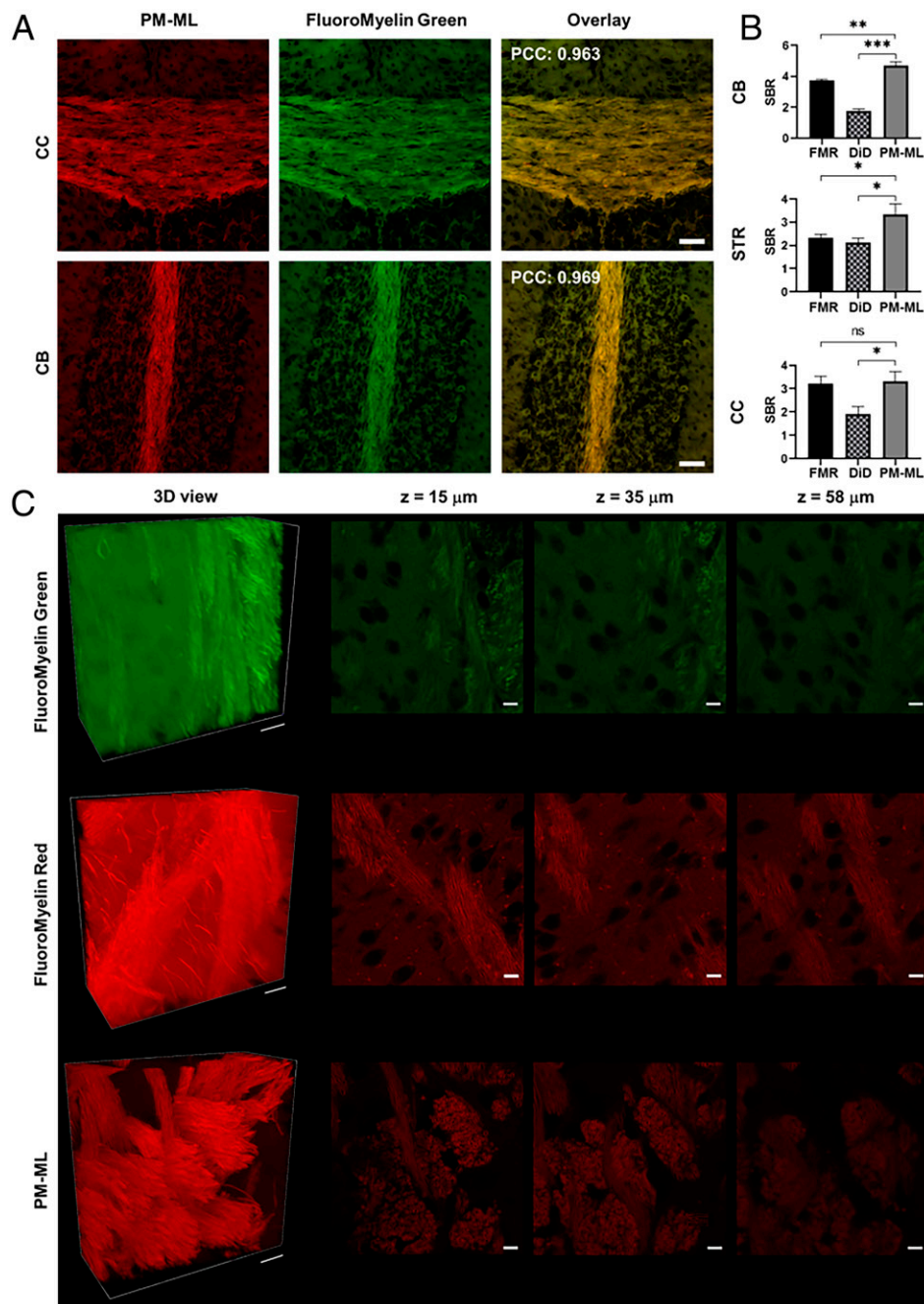
Fig. 4. (*A*) Brain regions rich in myelinated fibers (CC and CB) were costained with PM-ML (red) and FluoroMyelin Green. Both fluorescent probes colocalized with each other (yellow) with high Pearson's correlation coefficients (PCC). (Scale bars, 50 μm.) (*B*) Analysis of signal-to-background ratio (SBR) in the CC, STR, and CB of 500-μm-thick, cleared tissues (*Clear^T*) in the 10-mo-old C57BL/6J mouse brain stained by FluoroMyelin Red (FMR), DiD, and PM-ML, respectively. Statistical significance (ns: not significant, *$P < 0.05$, **$P < 0.01$, and ***$P < 0.001$) was assessed by two-way ANOVA test. The histogram shows the mean ± SD ($n = 3$). (*C*) 3D-rendered Z-stack of CPu in the ClearT mouse brain stained with FluoroMyelin Green, FluoroMyelin Red, or PM-ML from P18 C57BL/6J mice (63× objective, numerical aperature 1.4). (Scale bar in 3D view, 20 μm.)

observed, including the ventral STR in Fig. 5*A* which is associated with the reward-related reactivity (52), the ventral thalamus (Fig. 5*B*), the thalamocortical radiations crossing the CPu (*SI Appendix,* Fig. S16 *B*, *3*), the internal plexiform layer in the olfactory bulb and the wm in the CB (Fig. 5*C* and *SI Appendix,* Fig. S16 *B*, *1*), perforant path fibers in hippocampus, cerebral peduncle, middle cerebellar peduncle, medial longitudinal fasciculus in the midbrain (*SI Appendix,* Fig. S16 *B*, *2*), the pons (P), and the medulla oblongata (Fig. 5*D*). These observations demonstrated that PM-ML is a

reliable myelin probe which indistinguishably labeled myelinated fibers in different brain regions.

Given that the CB has a clear spatial pattern of whiter matter where myelinated nerve fibers are densely localized in, we then examined the staining pattern of PM-ML in the CB. In the mouse CB sections postfixed with paraformaldehyde and dehydrated with ethanol, PM-ML staining labeled the region interior to the cerebellar granule cells labeled by Hoechst 33342 (Fig. 5*C*). This is consistent with the typical spatial organization of myelinated axons in the wm. Compared with *Clear^{T2}*, *Clear^T* only uses
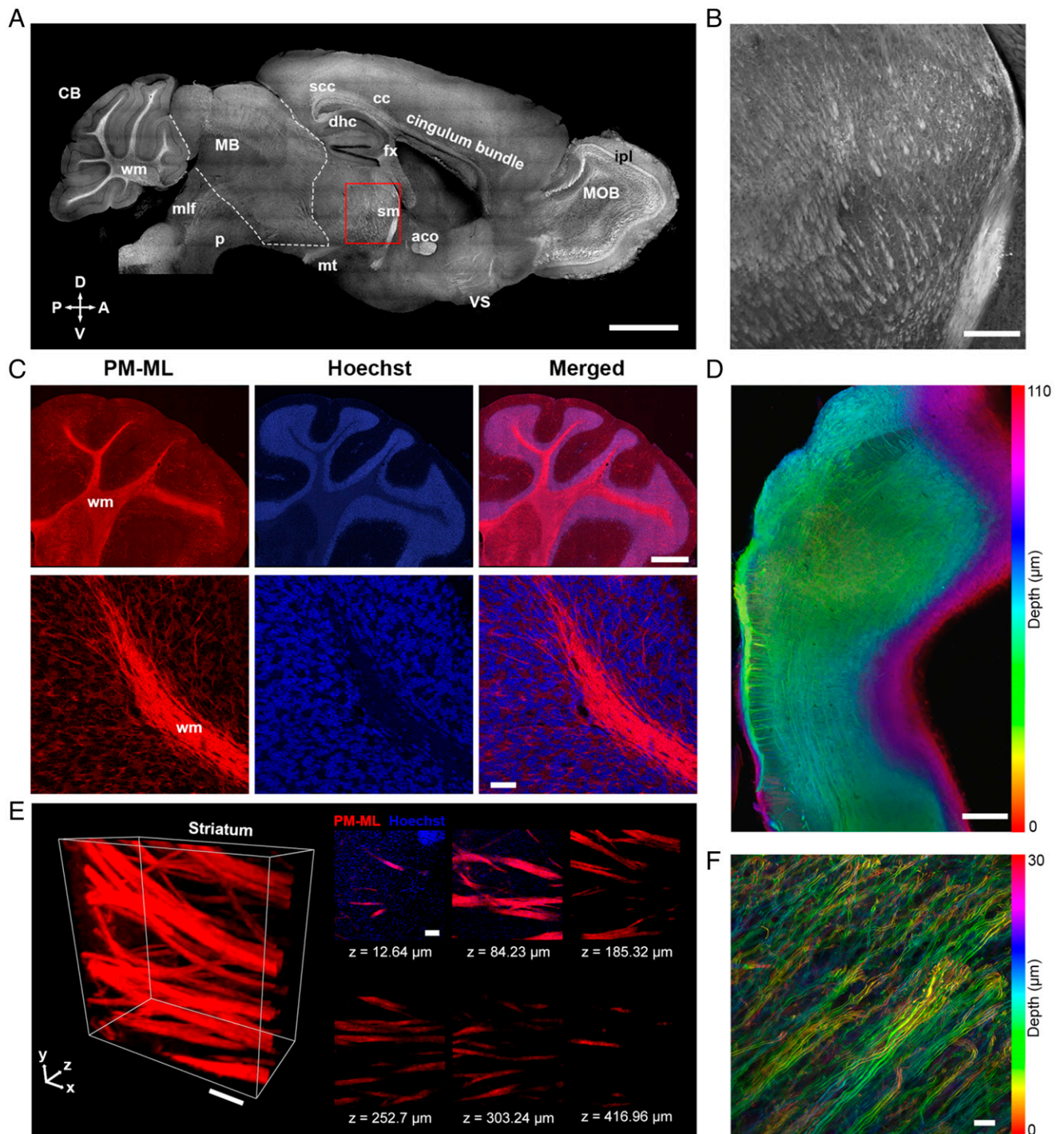
Fig. 5. (*A*) The stitched z-projections of the sagittal whole-brain section stained with PM-ML from a 16-wk-old C57BL/6J mouse. The brain was fixed with PFA and cleared with *Clear^T* to visualize myelinated tracts with the Nikon A1R HD25 confocal microscope (20×/0.75 NA objective). (Scale bar, 2 mm.) (*B*) Zoomed image of the ventral thalamus from the red box shown in *A*. (Scale bar, 300 μm.) (*C, Upper row*) Mosaic stitched image of PFA-fixed and ethanol-dehydrated CB stained with PM-ML and Hoechst 33342 (granule cells), cleared with *Clear^T2*. (Scale bar, 300 μm.) (*Lower row*) Z-stack image of myelinated fibers in the CB from the same sample recleared using the *Clear^T* method and acquired with the Zeiss LSM 880 microscope (20×/0.8 NA objective). (Scale bar, 50 μm.) (*D*) Color-coded z-projections of the P and medulla stained with PM-ML from the same sample in *A* under a 10×/0.75 NA objective. (Scale bar, 500 μm.) (*E*) 3D rendered Z-stack of the STR from the *Clear^T* mouse brain (10×/0.45 NA objective). (Scale bar in 3D view, 150 μm; Z tiles, 100 μm.) (*F*) The color depth–coded, high-magnification image of individual myelinated fibers from a PM-ML–stained tissue slab (63×/1.4 NA objective). (Scale bar, 10 μm.) Tissues from *C–F* were from 10-mo-old C57BL/6J WT mice. Abbreviations used are the following: CB, CC, splenium of the CC (scc), dorsal hippocampal commissure (dhc), fornix (fx), mammillothalamic tract (mt), stria medullaris (sm), aco, internal plexiform layer (ipl), wm, medial longitudinal fasciculus (mlf), ventral striatum (VS), P, and midbrain (MB).

formamide to improve the tissue transparancy, which is beneficial for viewing the fluorescent labeling of myelinated nerve fibers by high-resolution optical imaging. The re-clearing of the

PM-ML–stained, *Clear^T2*-cleared brain section with the *Clear^T* method not only kept the labeling specificity of PM-ML under the same imaging parameters but also further displayed the

projection of myelinated nerve fibers from GL to wm tracts (Fig. 5*C*). Furthermore, PM-ML retained its labeling selectivity in optically cleared tissues for further imaging after kept at 4 °C for 5 mo (*SI Appendix*, Fig. S17), but FluoroMyelin Red staining in tissues lost their selectivity during storage, and most of the fluorescence signal fade out in 3 wk (*SI Appendix*, Fig. S18). Therefore, PM-ML is compatible with the long-term storage of stained samples.

The P and the medulla oblongata are at close proximity to the thalamus and the aco. Several brain regions showing the most important part of the brainstem in which the reticular formation is responsible for the autonomic regulation, arousal, sleep and awareness, cognitive functions, etc. (53, 54). Besides, the myelinated corticospinal tract also descends from the motor cortex to the spinal cord via the brainstem (55). Myelination is important for brainstem functions, as myelin damage in the brain is associated with several neurological disorders such as central pontine myelinolysis (56, 57). In the z-stack projection of the sagittal section in the mouse brainstem, PM-ML staining showed pyramidal decussation in the caudal medulla where 90% of the descending fibers in the corticospinal tract cross the midline and continue along the cervical spinal cord (Fig. 5*D*). These observations demonstrate that PM-ML staining is also versatile in identifying myelinated fibers in the brainstem region.

Taking full advantage of PM-ML in myelin imaging, it was further utilized for practical applications in the 3D visualization of myelinated nerve fibers in the mouse brain. Multiple myelin

images of the STR in penetration depths of 500-μm thickness were reconstructed in 3D images (Fig. 5*E* and Movie S8). The fluorescence signal of PM-ML could still be detectable at the depth of 417 μm. Under a two-photon microscope, the imaging depth could reach more than 900 μm (*SI Appendix*, Fig. S19 and Movie S9). Meanwhile, the fine details of the myelinated fibers in the CB could also be acquired through 3D reconstruction from multiple images with high-resolution imaging. Individual myelinated axons could be traced in penetration depths of 30-μm thickness showing PM-ML labeling in the myelin sheaths (Fig. 5*F* and Movie S10). These results demonstrate that PM-ML is a promising NIR probe for deep-brain imaging at a cellular resolution which is compatible with multiple optical clearing methods in brain tissues.

Imaging Myelin Pathology in Cleared *Shiverer* Mouse Brain Sections. The *shiverer* mouse is a mouse model of demyelinating diseases such as multiple sclerosis. The myelin specificity of PM-ML and its practical applications in the study of demyelinating diseases was further validated using the *shiverer* mouse model. The *shiverer* mutation is a loss-of-function deletion–mutation in the myelin basic protein (MBP) gene (58). The deficiency of MBP, which is responsible for the adhesion of multilayered myelin membrane, will cause the loss of myelin sheath in the CNS (38). In comparing with the C57BL/6J WT control, the homozygous *shiverer* (Mbp^{shi}/Mbp^{shi}) mice had a complete loss of MBP expression in the brain (*SI Appendix*, Figs. S20 and S21). Despite that the heterozygous *shiverer* (Mbp^{shi}/Mbp^+) mice displayed
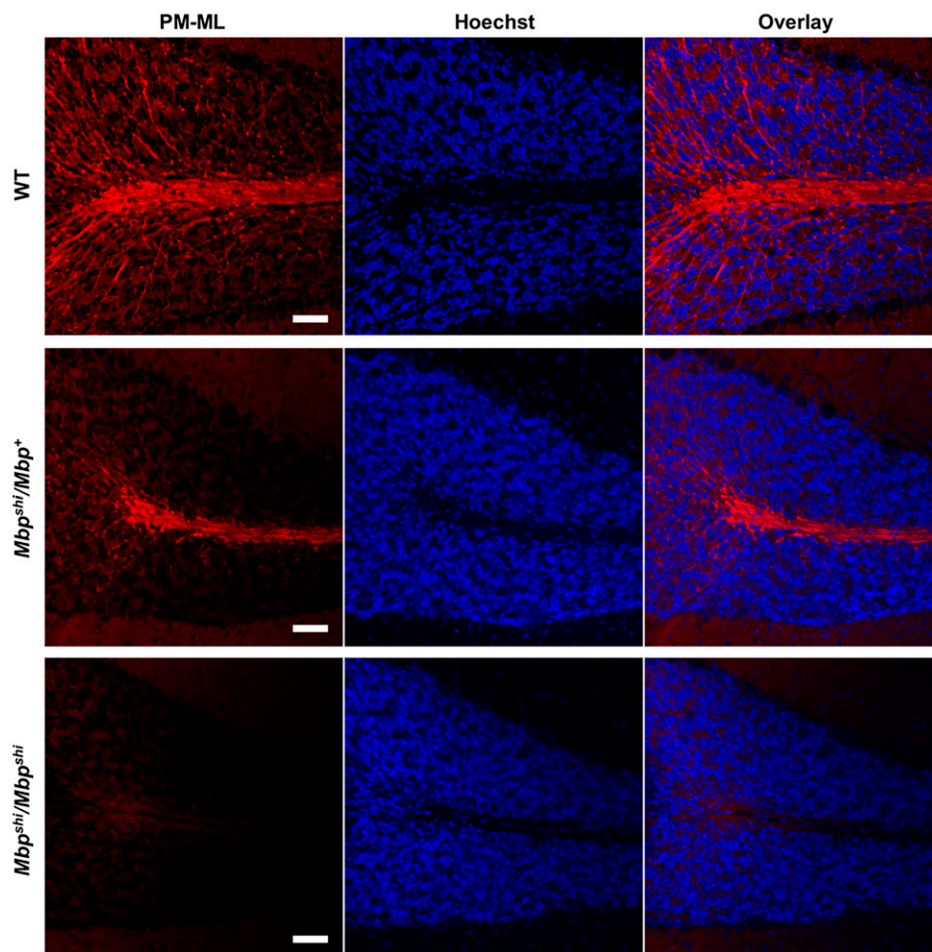
Fig. 6. PM-ML staining in cleared brain sagittal sections of 16-wk-old WT, *shiverer* heterozygous (Mbp^{shi}/Mbp^+), and *shiverer* homozygous (Mbp^{shi}/Mbp^{shi}) mice. Folia in CB regions were stained with PM-ML for myelin and with Hoechst 33342 for cerebellar granular cells. (Scale bars, 50 μm.)

Wu et al.
A near-infrared AIE fluorescent probe for myelin imaging: From sciatic nerve to the optically cleared brain tissue in 3D

PNAS | 7 of 9
https://doi.org/10.1073/pnas.2106143118

slightly lower MBP expression than the WT, it is reported that mild hypomyelination in Mbp^{shi}/Mbp^+ mice results in reduced myelin sheath thickness (59). In the sagittal sections of the 16-wk-old mouse brain, the WT mice showed typical myelinated axons projected from the cerebellar granule cell nucleus labeled by Hoechst 33342 (Fig. 6). In comparison, Mbp^{shi}/Mbp^+ mice had a weaker fluorescence signal of PM-ML, and Mbp^{shi}/Mbp^{shi} mice had a significant loss of PM-ML labeling in the wm (Fig. 6), suggesting that myelin is absent in the CB of Mbp^{shi}/Mbp^{shi} mice. These labeling patterns of PM-ML correlated well with the hypomyelination phenotypes of *shiverer* mice and demonstrated that PM-ML can be used in evaluating axonal myelination.

Concluding Remarks

In summary, an AIE-active NIR plasma membrane–targeting fluorescent probe named PM-ML with large Stokes shift and high brightness was rationally designed and easily synthesized with high yield. It had good biocompatibility and was able to selectively label the plasma membrane in both live and fixed cells with excellent photostability. PM-ML could be applied to the specific labeling of myelin fibers in mouse brain tissues and teased sciatic nerves with a high–signal-to-background ratio, compared with commercial probes FluoroMyelin Green/Red and DiD. It was adaptable to multiplexed tissue interrogation and compatible with multiple brain tissue clearing methods. PM-ML was stable and robust, keeping it bright and selective in cleared tissues for taking z-stack imaging, which required multiple times of scanning. Changing clearing methods from $Clear^{T2}$ to $Clear^T$ or keeping the stained samples for 5 mo for further imaging hardly affected its performance. Therefore, PM-ML is suitable for the 3D visualization of myelin sheaths and myelinated fibers and fascicles with high-penetration depth, and it can be used in assessing myelination in neuropathology in animal studies.

This study explicates a rational design of a myelin-specific AIE probe. The balanced hydrophobicity of the hydrophobic donor (D) and the hydrophilic acceptor (A) in PM-ML facilitates its targeting to the cell membrane through hydrophobic interaction and electrostatic interaction. The D–π–A structure also affords its long-wavelength emission. The nonplanar conformation of PM-ML contributes to its AIE properties. The NIR emission, a high selectivity to the cell membrane, and the AIE properties of the probe together result in a low background and high–signal-to-background ratio staining of the myelin structures. This design may provide a conceptual guideline for designing other myelin probes.

PM-ML is a versatile and reliable tool for visualizing myelinated fibers in the CNS and the PNS. It can provide a clearer image with high–signal-to-noise ratio to the researchers to better analyze myelin density, fascicular patterns, the trajectory of fiber tracts, as well as a detailed morphology of single-myelin fibers. We envision that the dye and the staining method have great potential for further application in neurological research to reveal the subtle myelin remodeling in development, disease progression, or treatment response. It is also expected that more AIE probes will be developed for neuroimaging. Images of the structures of the nervous system with high resolution and high contrast may be obtained with the help of the new imaging contrast agents and related techniques. This will bring us closer to understanding the brain's organization and functions.

Materials and Methods

Full experimental materials and procedures for the synthesis of compounds, molecular structures, spectroscopic characterization, cellular imaging, brain tissue imaging, genotyping, and Western blotting analysis are described in *SI Appendix*.

Data Availability. All study data are included in the article and/or supporting information.

1. L. Pedraza, J. K. Huang, D. R. Colman, Organizing principles of the axoglial apparatus. *Neuron* **30**, 335–344 (2001).
2. S. Poliak, E. Peles, The local differentiation of myelinated axons at nodes of Ranvier. *Nat. Rev. Neurosci.* **4**, 968–980 (2003).
3. D. K. Hartline, D. R. Colman, Rapid conduction and the evolution of giant axons and myelinated fibers. *Curr. Biol.* **17**, R29–R35 (2007).
4. X. Yin *et al.*, Evolution of a neuroprotective function of central nervous system myelin. *J. Cell Biol.* **172**, 469–478 (2006).
5. J. L. Dupree, J. A. Girault, B. Popko, Axo-glial interactions regulate the localization of axonal paranodal proteins. *J. Cell Biol.* **147**, 1145–1152 (1999).
6. C. Leterrier, P. Dubey, S. Roy, The nano-architecture of the axonal cytoskeleton. *Nat. Rev. Neurosci.* **18**, 713–726 (2017).
7. Y. Lee *et al.*, Oligodendroglia metabolically support axons and contribute to neurodegeneration. *Nature* **487**, 443–448 (2012).
8. D. Tkachev *et al.*, Oligodendrocyte dysfunction in schizophrenia and bipolar disorder. *Lancet* **362**, 798–805 (2003).
9. B. Huang *et al.*, Mutant huntingtin downregulates myelin regulatory factor-mediated myelin gene expression and affects mature oligodendrocytes. *Neuron* **85**, 1212–1226 (2015).
10. T. Philips, J. D. Rothstein, Glial cells in amyotrophic lateral sclerosis. *Exp. Neurol.* **262**, 111–120 (2014).
11. P. J. W. Pouwels *et al.*, Hypomyelinating leukodystrophies: Translational research progress and prospects. *Ann. Neurol.* **76**, 5–19 (2014).
12. J. M. Bin, D. A. Lyons, Imaging myelination in vivo using transparent animal models. *Brain Plast.* **2**, 3–29 (2016).
13. L. Frullano, C. Wang, R. H. Miller, Y. Wang, A myelin-specific contrast agent for magnetic resonance imaging of myelination. *J. Am. Chem. Soc.* **133**, 1611–1613 (2011).
14. A. J. Schain, R. A. Hill, J. Grutzendler, Label-free in vivo imaging of myelinated axons in health and disease with spectral confocal reflectance microscopy. *Nat. Med.* **20**, 443–449 (2014).
15. L.-A. Harsan *et al.*, Mapping remodeling of thalamocortical projections in the living reeler mouse brain by diffusion tractography. *Proc. Natl. Acad. Sci. U.S.A.* **110**, E1797–E1806 (2013).
16. H. Wang, Y. Fu, P. Zickmund, R. Shi, J.-X. Cheng, Coherent anti-stokes Raman scattering imaging of axonal myelin in live spinal tissues. *Biophys. J.* **89**, 581–591 (2005).
17. H. Lim *et al.*, Label-free imaging of Schwann cell myelination by third harmonic generation microscopy. *Proc. Natl. Acad. Sci. U.S.A.* **111**, 18025–18030 (2014).
18. J. Ben Arous *et al.*, Single myelin fiber imaging in living rodents without labeling by deep optical coherence microscopy. *J. Biomed. Opt.* **16**, 116012 (2011). Correction in: *J. Biomed. Opt.* **16**, 119802 (2011).
19. R. A. Hill, J. Grutzendler, Uncovering the biology of myelin with optical imaging of the live brain. *Glia* **67**, 2008–2019 (2019).
20. H. M. Lai, W.-L. Ng, S. M. Gentleman, W. Wu, Chemical probes for visualizing intact animal and human brain tissue. *Cell Chem. Biol.* **24**, 659–672 (2017).
21. W. Qin *et al.*, Facile synthesis of efficient luminogens with AIE features for three-photon fluorescence imaging of the brain through the intact skull. *Adv. Mater.* **32**, e2000364 (2020).
22. R. A. Hill, J. Grutzendler, In vivo imaging of oligodendrocytes with sulforhodamine 101. *Nat. Methods* **11**, 1081–1082 (2014).
23. E. Murray *et al.*, Simple, scalable proteomic imaging for high-dimensional profiling of intact systems. *Cell* **163**, 1500–1514 (2015).
24. Z. Xiang *et al.*, Detection of myelination using a novel histological probe. *J. Histochem. Cytochem.* **53**, 1511–1516 (2005).
25. J. Kilgore, "Lipophilic dyes and their application for detection of myelin." US Patent US 2006/0073541 A1 (2006).
26. P. C. Monsma, A. Brown, FluoroMyelin™ Red is a bright, photostable and non-toxic fluorescent stain for live imaging of myelin. *J. Neurosci. Methods* **209**, 344–350 (2012).
27. C. Wang *et al.*, Longitudinal near-infrared imaging of myelination. *J. Neurosci.* **31**, 2382–2390 (2011).

28. A. Nimmerjahn, F. Kirchhoff, J. N. D. Kerr, F. Helmchen, Sulforhodamine 101 as a specific marker of astroglia in the neocortex in vivo. *Nat. Methods* **1**, 31–37 (2004).
29. J. L. Salzer, Schwann cell myelination. *Cold Spring Harb. Perspect. Biol.* **7**, a020529 (2015).
30. H. J. Gruber et al., Anomalous fluorescence enhancement of Cy3 and cy3.5 versus anomalous fluorescence loss of Cy5 and Cy7 upon covalent linking to IgG and noncovalent binding to avidin. *Bioconjug. Chem.* **11**, 696–704 (2000).
31. R. T. K. Kwok, C. W. T. Leung, J. W. Y. Lam, B. Z. Tang, Biosensing by luminogens with aggregation-induced emission characteristics. *Chem. Soc. Rev.* **44**, 4228–4238 (2015).
32. S. Xu, Y. Duan, B. Liu, Precise molecular design for high-performance luminogens with aggregation-induced emission. *Adv. Mater.* **32**, e1903530 (2020).
33. X. Cai, B. Liu, Aggregation-induced emission: Recent advances in materials and biomedical applications. *Angew. Chem. Int. Ed. Engl.* **59**, 9868–9886 (2020).
34. Z. Guo, C. Yan, W.-H. Zhu, High-performance quinolone-malononitrile core as a building block for the diversity-oriented synthesis of AIEgens. *Angew. Chem. Int. Ed. Engl.* **59**, 9812–9825 (2020).
35. M.-Y. Wu et al., A small-molecule AIE chromosome periphery probe for cytogenetic studies. *Angew. Chem. Int. Ed. Engl.* **59**, 10327–10331 (2020).
36. L. Shi et al., An AIE-based probe for rapid and ultrasensitive imaging of plasma membranes in biosystems. *Angew. Chem. Int. Ed. Engl.* **59**, 9962–9966 (2020).
37. W. Fu et al., Rational design of near-infrared aggregation-induced-emission-active probes: In situ mapping of amyloid-β plaques with ultrasensitivity and high-fidelity. *J. Am. Chem. Soc.* **141**, 3171–3177 (2019).
38. Y.-L. Wang et al., Real-time fluorescence in situ visualization of latent fingerprints exceeding level 3 details based on aggregation-induced emission. *J. Am. Chem. Soc.* **142**, 7497–7505 (2020).
39. B. He, B. Situ, Z. Zhao, L. Zheng, Promising applications of AIEgens in animal models. *Small Methods* **4**, 1900583 (2020).
40. C. Liu et al., Near-infrared AIE dots with chemiluminescence for deep-tissue imaging. *Adv. Mater.* **32**, e2004685 (2020).
41. S. Wang et al., In vivo three-photon imaging of lipids using ultrabright fluorogens with aggregation-induced emission. *Adv. Mater.* **33**, e2007490 (2021).
42. D. Fitzner et al., Myelin basic protein-dependent plasma membrane reorganization in the formation of myelin. *EMBO J.* **25**, 5037–5048 (2006).
43. B. P. Bean, The action potential in mammalian central neurons. *Nat. Rev. Neurosci.* **8**, 451–465 (2007).
44. X. Luo et al., A general approach to the design of high-performance near-infrared (NIR) D-π-A type fluorescent dyes. *Chin. Chem. Lett.* **30**, 839–846 (2019).
45. M. Collot et al., MemBright: A family of fluorescent membrane probes for advanced cellular imaging and neuroscience. *Cell Chem. Biol.* **26**, 600–614.e7 (2019).
46. A. Shao et al., Insight into aggregation-induced emission characteristics of red-emissive quinoline-malononitrile by cell tracking and real-time trypsin detection. *Chem. Sci.* **5**, 1383–1389 (2014).
47. S. Xie, A. Y. H. Wong, S. Chen, B. Z. Tang, Fluorogenic detection and characterization of proteins by aggregation-induced emission methods. *Chem. Eur. J.* **25**, 5824–5847 (2019).
48. N. Elazar, E. Peles, Schwann-cell-derived CMTM6 restricts radial axonal growth. *Nat. Commun.* **11**, 5044 (2020).
49. J. Wen et al., Lentivirus-mediated RNA interference targeting RhoA slacks the migration, proliferation, and myelin formation of Schwann cells. *Mol. Neurobiol.* **54**, 1229–1239 (2017).
50. R. R. Llinás, K. D. Walton, E. J. Lang, "Cerebellum" in *The Synaptic Organization of the Brain*, G. M. Shepherd, Ed. (Oxford University Press, New York, 2004), pp. 271–310.
51. R. D. Fields, White matter matters. *Sci. Am.* **298**, 42–49 (2008).
52. T. Elvsåshagen et al.; Karolinska Schizophrenia Project (KaSP) consortium, The genetic architecture of human brainstem structures and their involvement in common brain disorders. *Nat. Commun.* **11**, 4016 (2020).
53. K. Koch et al., Association between white matter fiber structure and reward-related reactivity of the ventral striatum. *Hum. Brain Mapp.* **35**, 1469–1476 (2014).
54. J. Parvizi, A. Damasio, Consciousness and the brainstem. *Cognition* **79**, 135–160 (2001).
55. O. Raineteau, M. E. Schwab, Plasticity of motor systems after incomplete spinal cord injury. *Nat. Rev. Neurosci.* **2**, 263–273 (2001).
56. C. Rozeik, D. Von Keyserlingk, The sequence of myelination in the brainstem of the rat monitored by myelin basic protein immunohistochemistry. *Brain Res.* **432**, 183–190 (1987).
57. C. Lampl, K. Yazdi, Central pontine myelinolysis. *Eur. Neurol.* **47**, 3–10 (2002).
58. C. Readhead, L. Hood, The dysmyelinating mouse mutations shiverer (shi) and myelin deficient (shi^mld). *Behav. Genet.* **20**, 213–234 (1990).
59. S. Moore et al., A role of oligodendrocytes in information processing. *Nat. Commun.* **11**, 5497 (2020).

CHEMISTRY

NEUROSCIENCE

Wu et al.
A near-infrared AIE fluorescent probe for myelin imaging: From sciatic nerve to the optically cleared brain tissue in 3D